

Construction of Heterogenous S–C–S MoS₂/SnS₂/r-GO Heterojunction for Efficient CO₂ Photoreduction

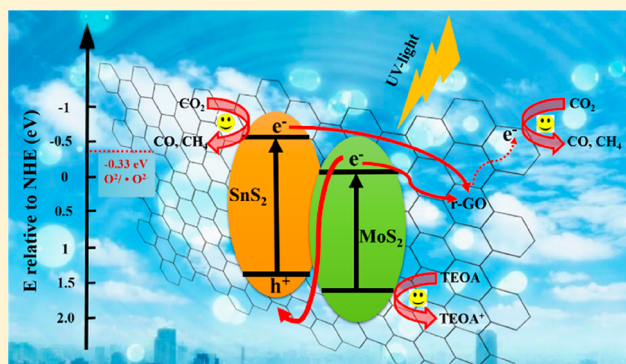
Shikang Yin,[†] Jinze Li,[†] Linlin Sun,[†] Xin Li,[†] Dong Shen,[†] Xianghai Song,[†] Pengwei Huo,^{*,†} Huiqin Wang,^{*,‡} and Yongsheng Yan[†]

[†]Institute of Green Chemistry and Chemical Technology, School of Chemistry and Chemical Engineering, Jiangsu University, Zhenjiang 212013, People's Republic of China

[‡]School of Energy and Power Engineering, Jiangsu University, Zhenjiang 212013, People's Republic of China

Supporting Information

ABSTRACT: Photocatalytic reduction of CO₂ by semiconductors is of great significance in generating value-added fuels. Here, we construct a novel S–C–S heterojunction constituted of MoS₂/SnS₂/r-GO by a simple solvothermal method. The prepared MoS₂/SnS₂/r-GO showed significant photoexcitation of photosensitive oxygen (ROS) by electron spin resonance spectroscopy, demonstrating that superoxide radicals ($\cdot\text{O}_2^-$), pores, and hydroxyl radicals ($\cdot\text{OH}$) are the main active species. The constructed S–C–S heterojunction has a multilevel electron transport mechanism and synergistic effect, which provides the possibility of producing more organic fuel. The photocatalytic materials were characterized by XRD, XPS, SEM, TEM, PL, etc. As a result, the atomic layer MoS₂/SnS₂/r-GO heterojunction exhibited a CO formation rate of 68.53 $\mu\text{mol g}^{-1} \text{h}^{-1}$ and a CH₄ formation rate of 50.55 $\mu\text{mol g}^{-1} \text{h}^{-1}$, respectively. This work opens up new prospects for the formation of heterojunctions of chalcogenide transition-metal sulfides.

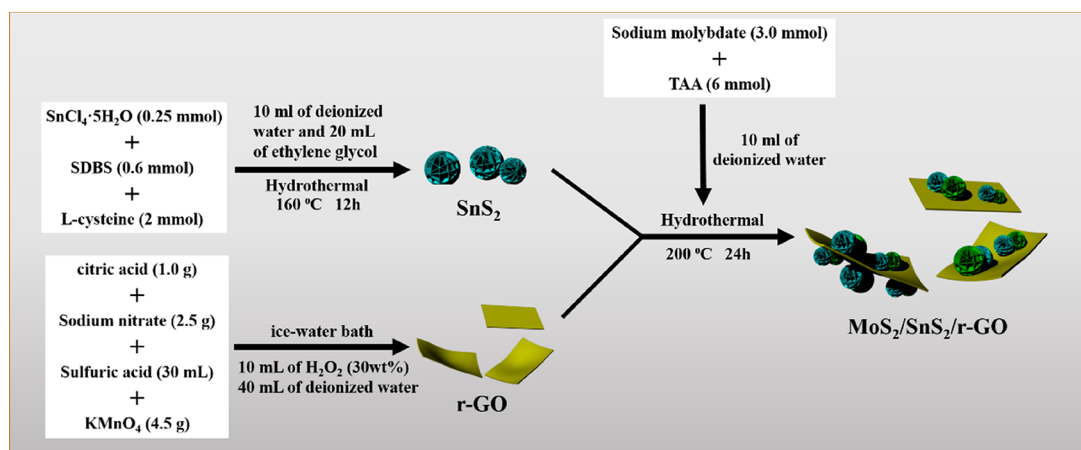


1. INTRODUCTION

Carbon dioxide (CO₂) is the main contributor to the greenhouse effect in the atmosphere, the rising concentration of which causes the radiation of infrared energy on the surface of the earth and brings about a series of problems: the increase in surface temperature rise causes global warming and sea level rise, the surrounding ecological balance and biodiversity has been destroyed, and there have been outbreaks of various diseases.^{1,2} Therefore, it is urgent to find a low-cost, pollution-free, and sustainable new energy to alleviate the consumption of fossil fuels.³ Biomass, wind, and solar energy are new sustainable energy sources. Among them, photocatalytic reduction technology is considered to be one of the most promising methods for solving the energy crisis due to its environmental friendliness, warm reaction conditions, low price, and clean and efficient advantages.⁴ An increasing number of researchers have invested a great deal of energy in researching efficient, renewable, and environmentally friendly photocatalysts.⁵ For the past few years, various promising semiconductors have been applied to photocatalytic reduction of CO₂, such as transition-metal oxides,⁶ polysulfides,⁷ etc. In order to capture CO₂, it is converted into valuable organic fuels such as methane (CH₄), carbon monoxide (CO), methanol (CH₃OH), etc.⁸ Among them, molybdenum disulfide (MoS₂) has attracted a great deal of attention from researchers due to its large specific surface area, plentiful abundance, low cost, and

other excellent properties.⁹ In addition, MoS₂ materials with unique structures and excellent properties are expected to be used in the fields of semiconductors, linear photoconductors, transistors, light-emitting devices, solar cells, supercapacitors, and the like to exhibit p-type or n-type conductivity.^{10–12} Nevertheless, MoS₂ still has shortcomings such as poor conductivity, low stability, and inclination for photocorrosion that have limited its application in artificial photosynthesis. On the basis of the above analysis, it is necessary to further improve and optimize molybdenum disulfide via adjusting the forbidden bandwidth, further enhancing the responsiveness to visible light, and improving stability to meet the practical needs of artificial photocatalysts. At present, some articles have been published on the latest optimization and improvement of MoS₂. For example, Yu et al.¹³ reported a MoS₂/TiO₂/Pt ternary composite with good photocatalytic hydrogen evolution activity, Fan et al.¹⁴ studied one kind of RP-MoS₂/r-GO photocatalyst with good ability for removal of Cr (VI) and organic contaminants, and Zhang et al.¹⁵ successfully prepared a MoS₂/Ti₃C₂T_x hybrid which has high electrocatalytic hydrogen evolution activity. Meanwhile, different dimensions of MoS₂ have been successfully prepared, such as MoS₂ quantum dots,¹⁶ three-dimensional MoS₂ nanoflower

Received: September 5, 2019

Scheme 1. Schematic Illustration of MoS₂/SnS₂/r-GO Nanocomposite Synthesis Process

balls,¹⁷ and two-dimensional ultrathin MoS₂ nanosheets.¹⁸ However, it is well-known that all of these photocatalysts have the disadvantages of short photogenerated carrier lifetime and high recombination rate.

Considering the problem of short lifetime and high recombination rate of the photogenerated carrier, reduced graphene oxide (r-GO) has attracted extensive attention from researchers thanks to its high specific surface area, high conductivity, and high carrier mobility.¹⁹ The introduction of r-GO can effectively increase carrier mobility and activity due to the p_z orbital of every carbon atom that is perpendicular to the layer plane and the large π bond of the atom constitutes a unique two-position network structure with a carrier mobility of about 15000 cm²/(V s) at room temperature.^{20,21} In order to further increase the activity of MoS₂/r-GO, we expect to find an outstanding material that combines with MoS₂/r-GO that can increase the performance of artificial materials more effectively. A combination of the main-group and transition-metal sulfides has rarely been reported in the photoreduction of CO₂; thus, the combination with main-group-metal sulfide semiconductor groups is a new strategy.

Atomic layer tin disulfide (SnS₂) is considered to be an extremely promising photocatalytic semiconductor thanks to its large specific surface area, high absorption coefficient, and good stability.²² In addition, the unique structure of the atomic layer level SnS₂ provides a rich functional active site.²³ Furthermore, a good conduction band position and a suitable band gap can both reduce CO₂ to a greater extent and make it more likely to absorb sunlight. Thus, it has received wide attention in various fields: Zhang et al.²⁴ successfully prepared ultrathin 2D SnS₂/C₃N₄ nanosheets for photodegradation of organic pollutants, Qu et al.²⁵ successfully prepared porous coral-like SnS₂ for the elimination of Cr(VI) in water, and Parveen et al.²⁶ successfully prepared SnS₂ of different shapes for high-performance supercapacitors. The storage performance of lithium batteries was studied by the synergistic effect of MoS₂/SnS₂ heterojunctions by Man et al.²⁷

Hence, we report a novel MoS₂/SnS₂/r-GO three-dimensional (3D) nanocomposite prepared by a solvothermal method, which photoreduced CO₂ under ultraviolet light. Interestingly, the MoS₂ assembled into 3D uniform nanoflower balls after a simultaneous coupling connection with r-GO and SnS₂.^{3,28} In our study, we have reduced the GO by hydrothermal methods.²⁹ Significantly, the introduction of

the carbon framework enables rapid carrier transfer, improving the overall efficiency of the photocatalyst. What is more, as a 2D support, r-GO can provide a platform to connect other semiconductors to form 3D nanostructures. This facilitates photocatalytic reduction of CO₂; the success can be attributed to more reactive sites being produced in comparison to 1D and 2D nanostructured materials.²⁴

In addition, a credible manufacturing mechanism is proposed on the basis of the current assembly process analysis. The 3D S–C–S heterojunction is formed by weak van der Waals interactions, and the large specific surface area and surface functional groups strengthen the synergistic effect of the interface; in addition, the unique structure of the same family of metal sulfides increases defects and reduces electron transport barriers, thereby promoting the transfer of electrons at the interface through electron tunneling and providing more active sites, reducing the barrier to photocatalytic reduction of CO₂. In addition, the high efficiency produces more organic fuel. The entire process of manufacturing 3D MoS₂/SnS₂/r-GO is shown in Scheme 1.

2. EXPERIMENTAL SECTION

2.1. Materials. Tin chloride pentahydrate (SnCl₄·5H₂O), thioacetamide (C₂H₅NS, TAA), sodium dodecyl benzenesulfonate (SDBS), L-cysteine (C₃H₇NO₂), potassium permanganate (KMnO₄), ethylene glycol (C₂H₆O₂), hydrogen peroxide (H₂O₂, 30%), hydrochloric acid (HCl, 5%), graphite powder, sodium nitrate (NaNO₃), ethanol (C₂H₅OH), and sulfuric acid (H₂SO₄) were all purchased from Sinopharm Chemical Reagent Co., Ltd. (Shanghai, China). Anhydrous sodium molybdate was purchased from Aladdin Reagent (Shanghai) Co., Ltd. All reagents used for preparation and direct use were of analytical grade and were not further purified. Deionized water from local sources was used in all experiments.

2.2. Synthesis of r-GO. r-GO was synthesized by a classical ice-water bath approach.³⁰ The process used microwave heating: graphite (1.0 g) and sodium nitrate (2.5 g) were dissolved in concentrated sulfuric acid (30 mL), and then potassium permanganate was slowly added. Then, 40 mL of deionized water and 10 mL of H₂O₂ (30 wt %) were also added directly. The prepared samples were centrifugally washed several times in water and ethanol and freeze-dried. The GO solution was quantified as 1.2 mg/mL.²⁹ The GO was treated by ultrasound (100 kHz, 500 W) for 2 h at room temperature until the solution was evenly dispersed. Then 0.5 mL of hydrazine hydrate and 20 mg of NaOH were added directly. After that, the solution was transferred to a 100 mL autoclave at 200 °C for 12 h. The powder was then freeze-dried.

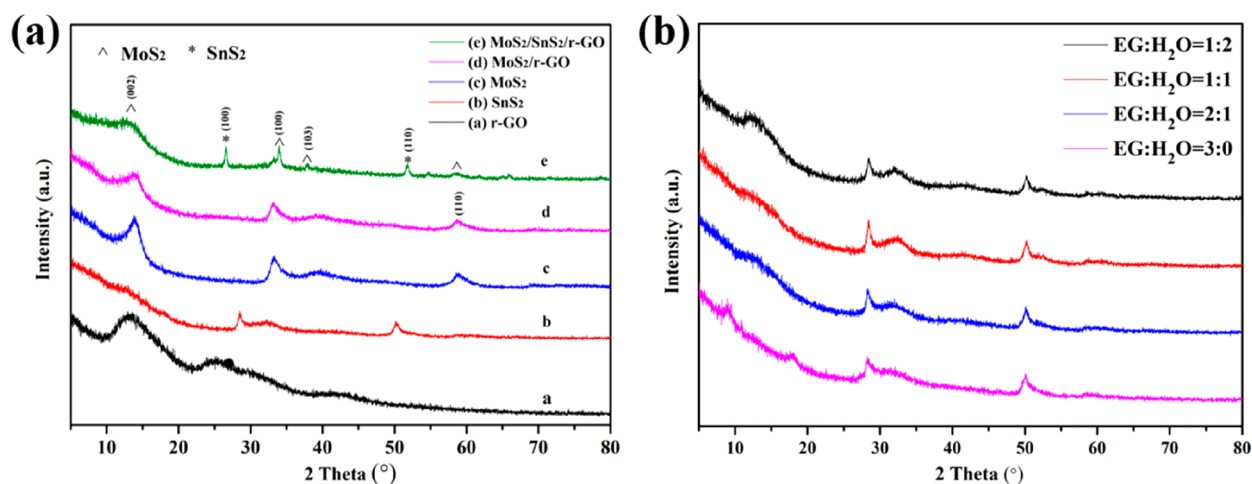


Figure 1. (a) XRD patterns of as-prepared r-GO, SnS₂, MoS₂, MoS₂/r-GO, and MoS₂/SnS₂/r-GO. (b) XRD patterns of different solvent ratios of as-prepared SnS₂.

2.3. Synthesis of Pineapple-Shaped SnS₂ with Hierarchical Three-Dimensional Architecture. A slight change was made to a typical modified water bath process:²² SnCl₄·5H₂O (0.25 mmol), sodium dodecyl benzenesulfonate (0.6 mmol), and L-cysteine (2 mmol) were dissolved in a mixed solution of 20 mL of ethylene glycol and 10 mL of deionized water, and the mixture was stirred for 10 min to form a uniform solution. Then, it was transferred to a 50 mL autoclave maintained at 160 °C for 12 h. An atomic layer of SnS₂ was prepared, and light yellow SnS₂ samples were collected, washed several times with deionized water and ethanol, and put in vacuum freeze-drying equipment until lyophilization for further characterization.

2.4. Synthesis of MoS₂/SnS₂/r-GO Composites. The synthesis of MoS₂/SnS₂/r-GO hybrid material was carried out by a solvothermal process. In the typical experimental process,⁷ a certain mass ratio of r-GO and ultrathin SnS₂ was simultaneously introduced in the preparation of MoS₂. The remaining steps are the same as those for making MoS₂. Finally, MoS₂/SnS₂/r-GO nanocomposites with different proportions of r-GO and SnS₂ to MoS₂ were prepared successfully.

2.5. Characterization. The crystal structure was examined with Ni-filtered Cu K α radiation by X-ray diffraction (XRD; MAC Science, Japan). The scan range 2 θ was 5–80° and the scan speed 5°/min. The measurements of X-ray photoelectron spectroscopy (XPS) were analyzed on a PerkinElmer PHI 5300 instrument to check the element status on the sample surface tested with a monochromatic Mg K α source. The high-resolution transmission electron microscopy (HR-TEM) and transmission electron microscopy (TEM) images and corresponding selected area electron diffraction (SAED) spectra were observed by transmission electron microscopy (JEM-2010, Japan). The scanning electron microscopy (SEM) images were characterized by a field emission scanning electron microscope (FE-SEM, JSM-7001F, Japan). The catalyst was subjected to ultraviolet–visible diffuse reflectance spectroscopy (DRS) measurements using a Shimadzu UV-3600 spectrometer, performed in the test zone of 200–800 nm and using BaSO₄ as a reference. The photoluminescence (PL) spectra for solid powders were carried out with an F-4500 instrument (Hitachi, Japan) and a xenon (Xe) lamp with an excitation wavelength of 345 nm.

2.6. Photoelectrochemical Test. The electrochemical system (CHI 660B, Shanghai, China) used a standard three-electrode quartz cell containing 0.5 M Na₂SO₄ electrolyte solution, and a Pt wire and a saturated calomel electrode (SCE) were used as a counter electrode and a reference electrode, respectively. The process of working electrode preparation was as in previous studies. Electrochemical impedance spectroscopy (EIS) was performed in a 0.5 M Na₂SO₄ solution at a frequency from 0.1 Hz to 100 kHz and 0.5 V. The sinusoidal potential amplitude applied in every case was 5 mV, which

was performed using an electrochemical workstation, and all electrochemical signals were recorded with a CHI660B electrochemical analyzer (Chen Hua Instruments, Shanghai, China).

2.7. Photocatalytic Reduction CO₂ Experiments. In order to compare the photocatalytic reduction properties of pure MoS₂, different contents of synthetic MoS₂/r-GO, and different contents of synthetic MoS₂/SnS₂/r-GO composites, a series of CO₂ photo-reduction ability tests were carried out on the prepared samples. Under the irradiation of ultraviolet light, a 300 mL closed photochemical reactor was used, adopting 8 W mercury lamp as the light source for the photocatalytic reaction. In addition, 20 mg of the photocatalyst, 100 mL of NaOH (0.1 M) solution, and a given mass of triethanolamine (TEOA) were placed in the reactor system, and the mixture was stirred under strong magnetic force for 10 min to homogenize the solution. CO₂ (99.999%) gas was bubbled for 20 min to exhaust air, and then the system pressure was maintained at 1.4 × 10⁵ Pa. Photocatalytic materials were taken from the enclosed light at 60 min intervals. The type and content of the product were measured every 1 h by a gas chromatography (GC-7920, China) detector. The isotope-labeling experiments were performed using ¹³CO₂ instead of ¹²CO₂, and the products were analyzed using gas chromatography–mass spectrometry (GC-MS, 7890A and 5975C, Agilent).

3. RESULTS AND DISCUSSION

3.1. Compositional and Crystal Structure Information. Figure 1a shows the XRD patterns of SnS₂, MoS₂, MoS₂/r-GO, and MoS₂/SnS₂/r-GO with different SnS₂ loading amounts and different r-GO loading amounts. The distinct peaks located at ca. 13.51, 33.95, 39.03, and 58.68° are indexed to the (002), (100), (103), and (110) crystal planes of MoS₂. The distinct peaks located at ca. 26.49 and 51.61° are indexed to the (100) and (110) crystal planes of the SnS₂ phase with lattice constants of $a = 3.05$ Å and $c = 1.82$ Å (JCPDS 40-1467).^{14,23,31} The results show that all of the diffraction peaks of MoS₂ conform to the standard XRD pattern of the MoS₂ structure, and the lattice constants are $a = 6.09$ Å, $b = 2.63$ Å, and $c = 1.581$ Å (JCPDS 17-0744),³² whereas no typical diffraction peaks of r-GO were detected on account of the limited amounts of r-GO in the MoS₂/r-GO composites, the change in r-GO fraction, and the diffraction peak of MoS₂ decreasing slightly; similar results have been reported elsewhere.¹⁴ However, when the semiconductor SnS₂ is added, the intensity and position of other diffraction peaks are significantly changed while the SnS₂ diffraction peak appears, indicating the successful synthesis of ternary composites.

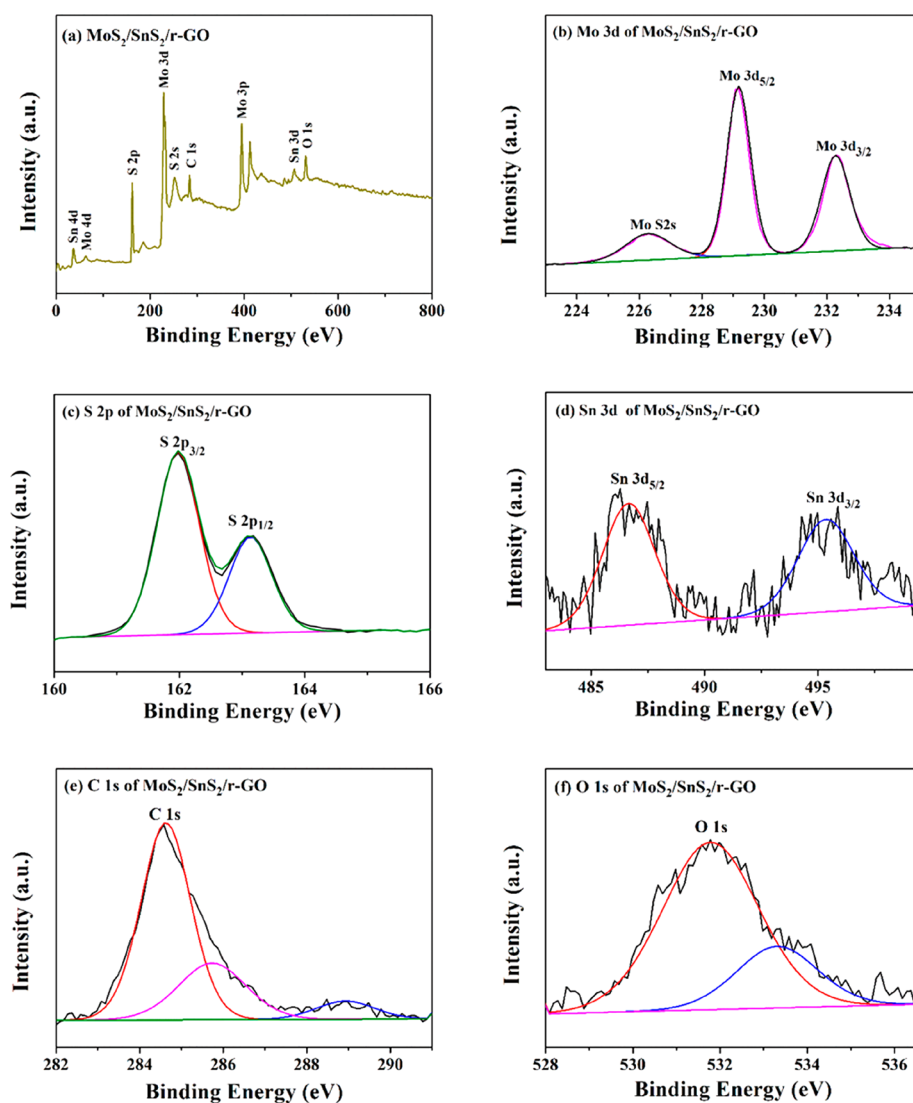


Figure 2. XPS spectra of (a) survey, (b) Mo 3d, (c) S 2p, (d) Sn 3d, (e) C 1s, and (f) O 1s of MoS₂/SnS₂/r-GO.

Figure 1b shows the XRD patterns of different solvent ratios of SnS₂.

To further determine the existence of MoS₂ and SnS₂, the surface electronic state, elemental composition, and bonding state of the synthesized samples were examined by XPS tests. The measured full spectrum (**Figure 2a**) confirmed the presence of Mo, S, Sn, C, and O elements in the sample, and the peaks of Mo 3d, S 2p, Sn 3d, C 1s, and O 1s appeared at their standard positions. As shown in **Figure 2b**, the Mo 3d spectrum has three different peaks, with peaks centered at 229.1 and 232.3 eV attributed to Mo 3d_{5/2} and Mo 3d_{3/2},²⁷ respectively. In addition, the binding energy of the Mo S2s peaks is at 226.3 eV.¹² In **Figure 2c**, the peaks at binding energies centered at about 161.77 and 163.16 eV are ascribed to S 2p_{3/2} and S 2p_{1/2},^{10,23,33} respectively. The binding energy positions of Mo and S are consistent with those reported previously. In **Figure 2d**, the two peaks at 486.7 and 495.3 eV in the Sn spectrum belong to Sn 3d_{3/2} and Sn 3d_{5/2},^{23,34} respectively, further illustrating the coexistence of Sn⁴⁺ and Mo⁴⁺ in the compound. The C 1s electron energy spectrum is shown in **Figure 2e**. The high-resolution XPS spectral binding energy of C 1s at 284.6 eV shows a main peak indicating C–C or C=C with an sp² orbital.³⁵ The binding energies of three

peaks at 284.5, 285.7, and 287.8 eV can be assigned to C–S bonds, C–O bonds, C=O bonds or O–C=O bonds, revealing surface functional groups on r-GO.^{14,36} For the O 1s core level spectrum in **Figure 2f**, the two peaks fitted by the O 1s spectrum are located at 531.78 and 533.41 eV.^{37,38} The above XPS analysis further indicates that the S–C–S heterojunction was successfully synthesized, and r-GO may act as a bridge for transporting carriers of the electron channel. This result is consistent with XRD.

3.2. Raman Analysis. The prepared photocatalysts were characterized by Raman spectroscopy. The crystallinity, local structure, and bonding state of the catalyst were studied. **Figure 3** shows the Raman spectrum of the synthesized photocatalysts. All samples are well crystallized in a monoclinic structure, which is consistent with the XRD results. As shown in **Figure 3**, for pure SnS₂, a distinct band appeared at 307 cm⁻¹, corresponding to the typical A_g vibration mode of the SnS₂ material.³⁴ Interestingly, the band of SnS₂ moved upward from 307 to 310 cm⁻¹ in the composite. It is speculated that the red shift may be due to the insertion of Mo⁴⁺. Theoretically, the Mo⁴⁺ radius is larger than the Sn⁴⁺ radius; thus, the bonding force constant of Mo–S should be smaller, which may result in a red shift of the SnS₂ lattice vibration.^{39,40}

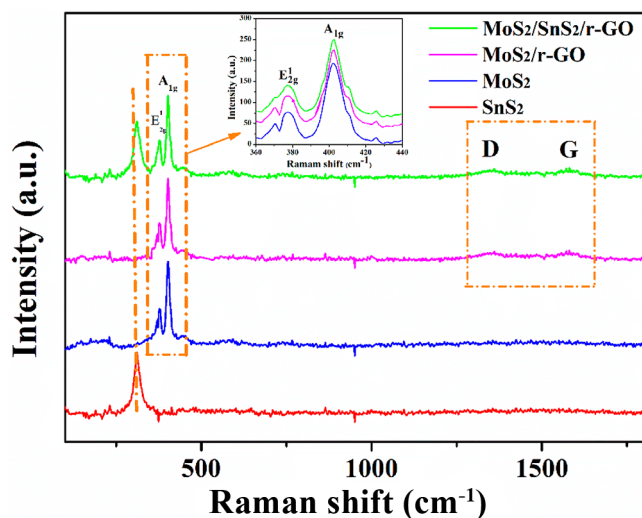


Figure 3. Raman spectra of SnS₂, MoS₂, MoS₂/r-GO, and MoS₂/SnS₂/r-GO, respectively.

In addition, the other two main bands at 377 and 401 cm⁻¹ can correspond to the E_{2g}¹ and A_{1g} modes of MoS₂, respectively. It is well-known that the E_{2g}¹ mode corresponds to the in-plane opposite vibration of two S atoms with respect to Mo atoms, while the A_{1g} mode is related to the out-of-plane vibration of the S atoms in the opposite direction,⁴¹ and they were both highly sensitive to tensile or compressive strain. For the composites, a slight red shift (1 cm⁻¹) of the A_{1g} mode was also observed. The lattice spacing mismatch of MoS₂/SnS₂ between MoS₂ and SnS₂ may change the local strain on the surface of the MoS₂ nanoflower balls, resulting in a red shift (1 cm⁻¹) of the A_{1g} band.¹¹ Moreover, the rest of the modes were derived from the 1350.1 cm⁻¹ defect-induced D band and the 1580.5 cm⁻¹ symmetrically allowed G band. Furthermore, the I_D/I_G ratios of MoS₂/r-GO (1.28) and MoS₂/SnS₂/r-GO (1.32) are both larger than that of GO (1.13);^{42,43} this indicates that GO is accurately reduced to r-GO during the synthesis. Obviously, this is consistent with the XRD.

3.3. UV–Vis DRS Analysis. The light absorption capacity of photocatalysts was studied by UV–vis spectrophotometry. Figure 4a shows the UV–vis diffuse reflectance spectra of SnS₂, MoS₂, MoS₂/r-GO, and MoS₂/SnS₂/r-GO samples. The

Kubelka–Munk equation was applied to measure the optical band gap (E_g), and then a plot was obtained via the transformation based on $[F(R_{\infty})h\nu]^{1/2} - h\nu$ for direct band gap semiconductors.³⁷ The pure MoS₂ sample showed strong optical absorption in the UV light region, and an absorption mutation occurred at about 347 nm, corresponding to a forbidden bandwidth of about 1.78 eV.⁴⁴ Different from the pure MoS₂ absorption behavior, the obtained MoS₂/SnS₂/r-GO composite exhibits a strong absorption peak and a wide visible light absorption range, which is caused by the introduction of SnS₂.¹⁴ The absorption shift occurred at around 330–450 nm, which indicated its enhanced visible light induced the photocatalytic activity.⁴⁵ It is worth noting that the visible light collection of MoS₂/SnS₂/r-GO composites is significantly increased in comparison with that of pure MoS₂ and MoS₂/r-GO, obviously demonstrating that the enhanced light absorption of MoS₂/SnS₂/r-GO composites can be effectively utilized and thus result in the production of more carriers under the similar illumination.^{46,47} In addition, the effective mass was deduced at the top of the valence band and the bottom of the conduction band from the band structure.⁴⁸ In particular, the relative energy levels of the valence band maximum (VBM) and the conduction band minimum (CBM) play an important role in the redox capability of photocarriers in the system.⁴⁹ To further determine the band structure of the prepared material, an XPS valence band spectrum was obtained. As shown in Figure 4b, the highest occupied electron state densities measured were 1.61 and 1.46 eV, which matched values for the initial MoS₂ and SnS₂ by XPS. The ternary composite material has a significant red shift phenomenon, manifesting that the introduction of SnS₂ does alter the electronic density of the MoS₂ matrix. This also means that SnS₂ doping into MoS₂ may cause an electro-negative defect state.⁵⁰

3.4. Morphological Analysis. The crystal form and morphology of the prepared samples were determined by mapping images with TEM, HRTEM, SEM, and EDX elements. Figure 5a,b shows TEM images of the obtained MoS₂ and r-GO, respectively. It is shown that the obtained MoS₂ is aggregated to form flowerlike spherical nanoparticles and thin r-GO. As shown in Figure 5c, the carbon-incorporated MoS₂/r-GO clearly appears as petal-like shapes on r-GO. Figure 5d shows a TEM image of the prepared MoS₂/SnS₂/r-

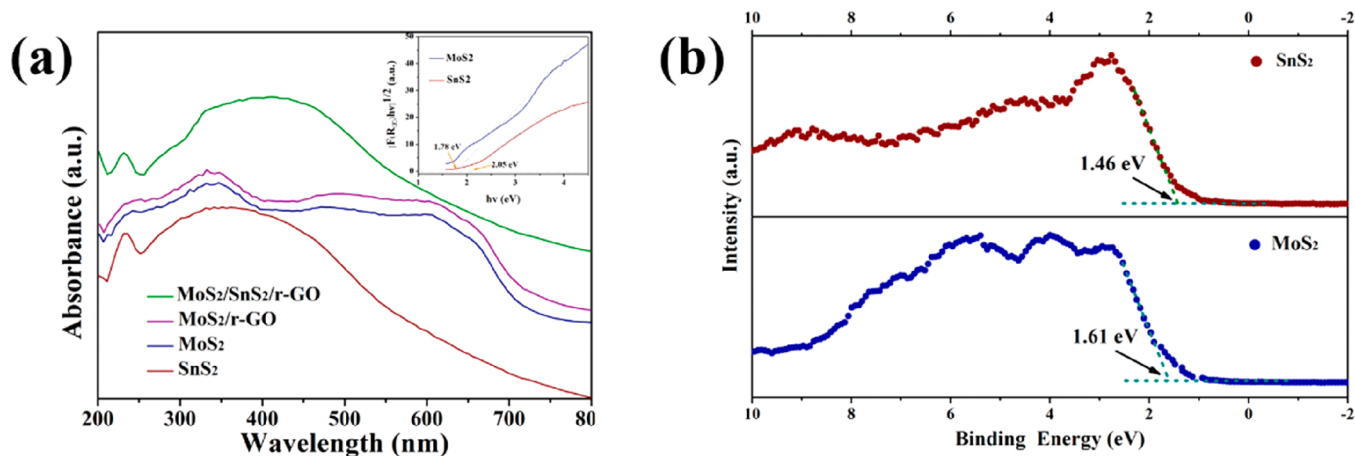


Figure 4. (a) UV–vis diffuse reflectance spectra of as-prepared SnS₂, MoS₂, MoS₂/r-GO, and MoS₂/SnS₂/r-GO. Inset: forbidden bandwidths of the corresponding samples. (b) XPS valence band spectra of pure MoS₂ and pure SnS₂.

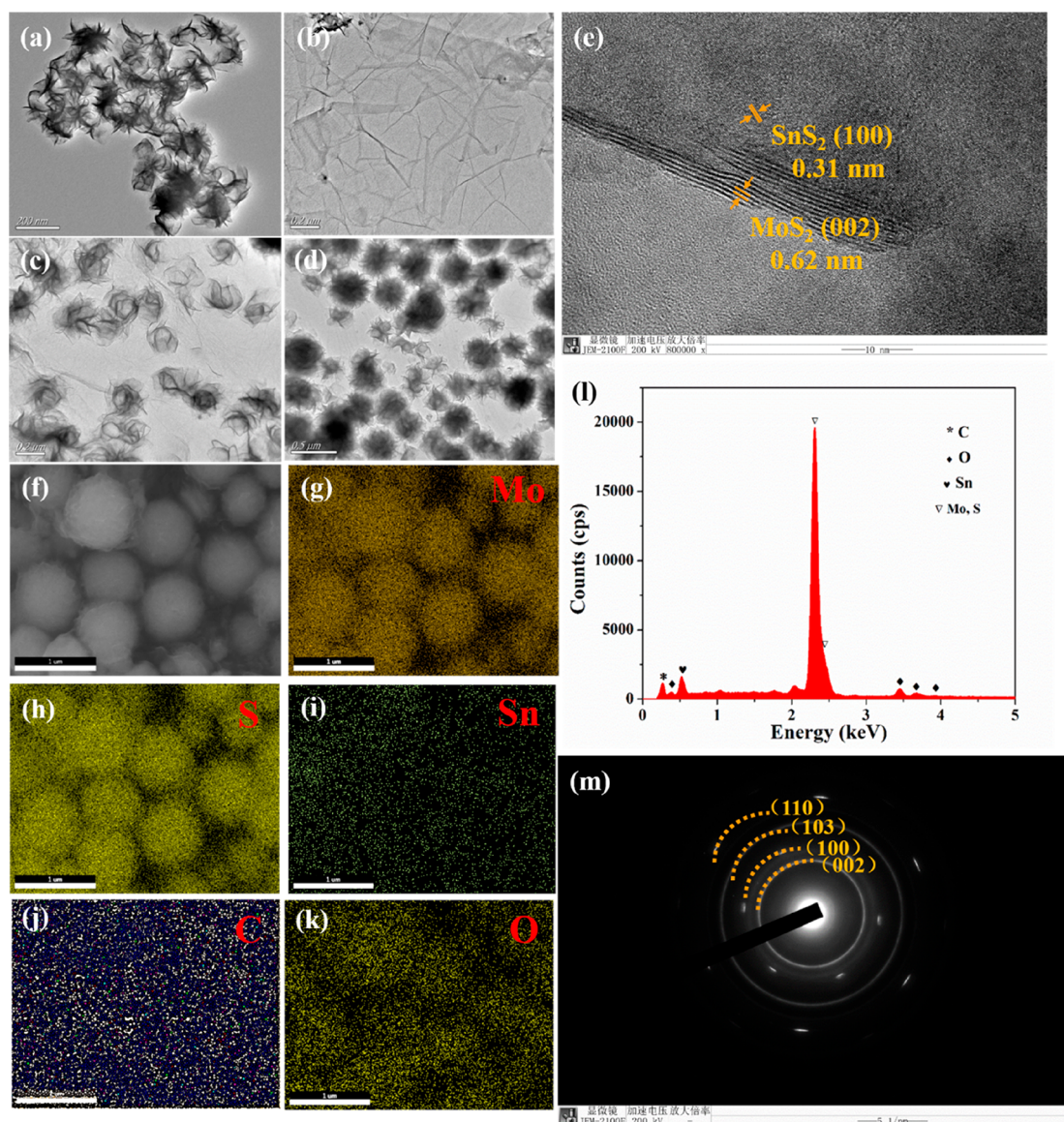


Figure 5. Morphology of the as-prepared MoS₂/SnS₂/r-GO blocks. TEM images of the MoS₂ particles (a), r-GO (b), MoS₂/r-GO (c), MoS₂/SnS₂/r-GO (d). HRTEM image of the MoS₂/SnS₂/r-GO heterostructure (e). SEM image (f) and EDX elemental mapping (g–k) of MoS₂/SnS₂/r-GO. EDX analysis (l) and SAED pattern (m) of MoS₂/SnS₂/r-GO.

GO, which has excellent dispersibility, and the prepared sample retains a favorable small-sized petal-like morphology after r-GO modification.^{42,51} The HRTEM image is as shown in Figure 5e, and the crystal structure and heterojunction of the prepared MoS₂/SnS₂/r-GO can be clearly observed, so that it is well matched with MoS₂ and SnS₂; the lattice spacings are 0.62 and 0.31 nm, respectively. They correspond to the (002) crystal plane of the typical MoS₂ and the (100) crystal plane of SnS₂.^{24,52} The EDX analysis and SEM images of MoS₂/SnS₂/r-GO are shown in Figure 5f–l. The distributions of Mo, S, Sn, C, and O elements (Figure 5g–l) are shown in the EDX mapping images to further confirm the successful preparation of the nanocomposite. Furthermore, the SAED characterization of MoS₂/SnS₂/r-GO with a scattering diffraction pattern and concentric rings (Figure 5m) shows that MoS₂/SnS₂/r-GO exhibits a nanoscale polycrystalline structure, which is consistent with the XRD results.¹⁴ The successful preparation of the S–C–S heterojunction was further confirmed.

3.5. PL Spectra. The photocatalytic activity of the sample was investigated by photoluminescence spectroscopy, and light-induced electron–hole pair migration and recombination processes on each sample were found. Because PL emission is a free vector recombination,^{37,53,54} Figure 6 shows the steady-state PL spectra of pure MoS₂, pure SnS₂, MoS₂/r-GO, and MoS₂/SnS₂/r-GO samples. The pure MoS₂ material exhibits strong light emission at 429 nm excitation, which mainly results from the the high recombination of electrons of MoS₂.⁵⁵ In addition, the PL signal strength of pure MoS₂ is higher than that of the MoS₂/r-GO composite, indicating that the composite probability of the MoS₂/r-GO photogenerated carrier recombination rate is lower. After the introduction of SnS₂, the PL intensity of MoS₂/SnS₂/r-GO composites is significantly lower than that of MoS₂/r-GO, the lifetime of the electron–hole pairs is extended, and the recombination rate of the electron–hole pair is reduced; this lower rate means that the MoS₂/SnS₂/r-GO composite has higher photocatalytic activity. This phenomenon is attributed to the high electron

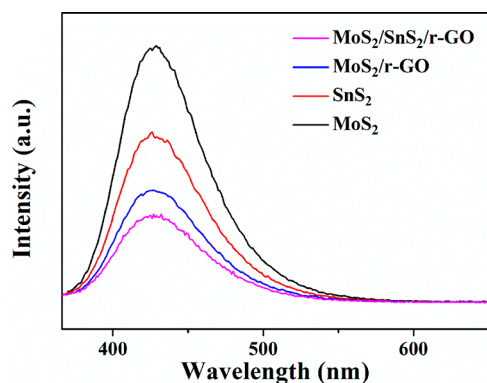


Figure 6. PL emission spectra of MoS₂, SnS₂, MoS₂/r-GO, and MoS₂/SnS₂/r-GO.

transport of the spatially extended p-bond conjugated system of SnS₂.^{22,56} At the same time, r-GO significantly accelerates the generation of charge-transfer hybrid materials through an effective interface. The electron transfer (ET) process reduces the recombination of e/h⁺ pairs in the MoS₂/SnS₂/r-GO interface layer.^{51,57,58} On the basis of the above analysis, the MoS₂/SnS₂/r-GO composite photocatalyst exhibited excellent photocatalytic activity.

3.6. Electrochemical Properties Analysis. In order to investigate the photoelectrochemical properties of the obtained samples, photoelectrochemical analysis was carried out with an electrochemical workstation to detect the separation efficiency of the photogenerated charge carriers. Photoelectric response and EIS measurements are shown in Figure 7a,b. The transient photocurrent response of pure MoS₂, pure SnS₂, MoS₂/r-GO, and MoS₂/SnS₂/r-GO in several open–close cycles under visible light irradiation ($\lambda > 420$ nm) were measured in 0.5 M Na₂SO₄ solution. MoS₂/10% SnS₂/3% r-GO exhibits a strong transient photocurrent response, which was approximately 2 times that of MoS₂/3% r-GO and 4 times that of MoS₂ (Figure 7a). The results show that r-GO plays a crucial role in effective charge transport. In addition, the good photoresponse of SnS₂ is one of the reasons for the higher photocurrent response, resulting in a significant increase in the separation of light-generated e/h⁺ pairs in composites.⁵⁹ The EIS Nyquist test (frequency 0.1 Hz to 100 kHz, 0.5 V) as shown in Figure 7b.

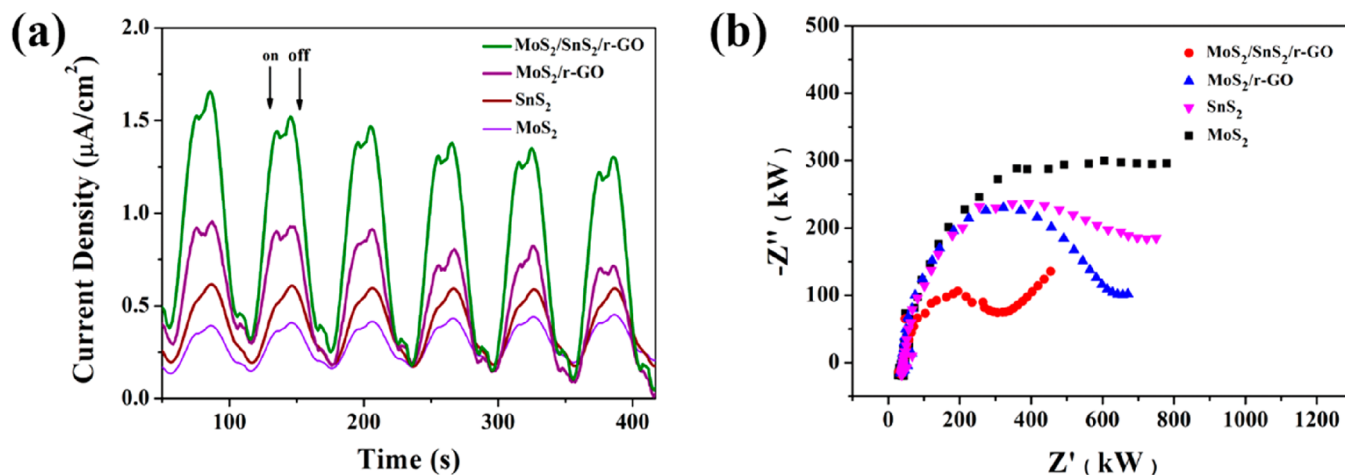


Figure 7. Transient photocurrent response (a) and EIS Nyquist plots (b) of MoS₂, SnS₂, MoS₂/r-GO, and MoS₂/SnS₂/r-GO nanocomposites under visible light irradiation.

The arc radius of the MoS₂/SnS₂/r-GO electrode is smaller than the arc radius of the original MoS₂, SnS₂, and MoS₂/r-GO electrodes, indicating that the surface reaction speed of the working electrode is faster, the charge recombination rate is lowered, and the effective migration of electrons and holes is improved,^{54,60} the results corresponded to the results of the photoluminescence spectrum. The entire composite photocatalytic system is more efficient.

3.7. Analysis of Reactive Species. To determine the possible mechanism, the samples were tested for ESR. Moreover, the most directly validated detection technique for detecting short-lived free radicals and paramagnetic materials is the use of ESR spin capture and spin labeling techniques for MoS₂, MoS₂/r-GO, and MoS₂/SnS₂/r-GO nanomaterials under UV–vis light illumination.⁵⁰ Each ROS and electron/hole generated under excitation conditions is identified. Here, we chose 5,5-dimethyl-1-pyrroline *N*-oxide (DMPO) and water (H₂O) as solvents for the detection of hydroxyl radicals ($\cdot\text{OH}$) and superoxide radicals ($\cdot\text{O}_2^-$), respectively.⁶¹ Figure 8 gives ESR spectra of various traps in MoS₂, SnS₂, MoS₂/r-GO, and MoS₂/SnS₂/r-GO hybrid materials before and during simulated sunlight exposure. For comparison, the same experiment was performed on different materials. It is obvious that there is no peak in Figure 8 before the light is on. However, when light is irradiated, the characteristic peaks appear rapidly in the spectra of MoS₂, SnS₂, MoS₂/r-GO, and MoS₂/SnS₂/r-GO in Figure 8, such as a typical 1:2:2:1 quadruple feature spectrum and observed distinct features corresponding to hydroxyl radicals (DMPO- $\cdot\text{OH}$) and superoxide radicals (DMPO- $\cdot\text{O}_2^-$), respectively, and the intensities of hydroxyl radicals and superoxide radicals change significantly.^{62,63} This result signifies that photogenerated electrons can react with oxygen to generate $\cdot\text{O}_2^-$ radicals.^{17,64} Next, these samples detected that DMPO- $\cdot\text{OH}$ radicals were acquired by further reaction of $\cdot\text{O}_2^-$ radicals with electrons and H⁺, where H⁺ was derived from the ionization process of H₂O.⁶⁵ The strengths of the peaks of these two radicals are obviously enhanced by the introduction of r-GO and SnS₂,⁶⁶ respectively, This is indirect proof that the photocatalytic activity of MoS₂/SnS₂/r-GO composite is better than that of pure MoS₂, SnS₂ and MoS₂/r-GO.

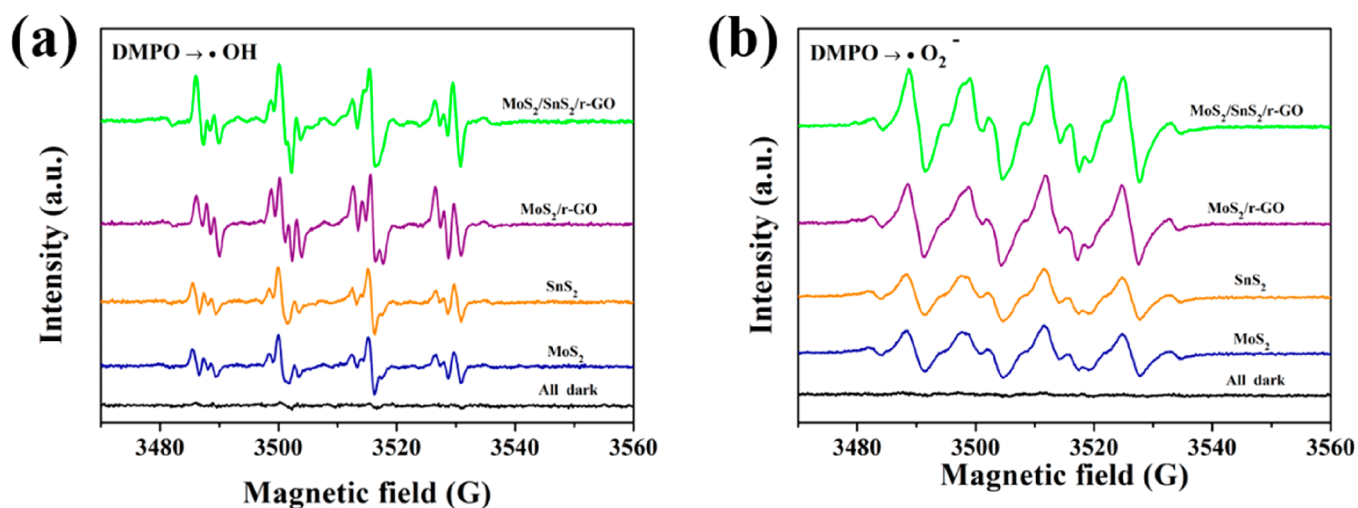


Figure 8. (a) DMPO spin-trapping ESR spectra of MoS₂, SnS₂, MoS₂/r-GO, and MoS₂/SnS₂/r-GO in an aqueous dispersion and (b) in a methanol dispersion.

3.8. Photocatalytic Reduction of CO₂. The photocatalytic activity of these samples was examined by using photoreduction equipment, with CO₂ as the simulated reactant. Gas-phase products were identified and quantitatively analyzed by gas chromatography (GC). Prior to the photocatalytic test, the adsorption and desorption equilibria of all samples were achieved by stirring in the dark for 20 min without air and magnetic force. Control experiments showed that CO and CH₄ were not detected in the dark or in the absence of carbon dioxide, indicating that CO₂ produced CO and CH₄ under ultraviolet light under the action of the catalysts. With the addition of different proportions of SnS₂ semiconductors, the photocatalytic activity is significantly improved due to better synergistic effects. The optimal photocatalytic activity of MoS₂/SnS₂/r-GO has been determined to be quantitatively 3% r-GO and 10% SnS₂. It can be seen from Figure 9a–d that the yields of CO and CH₄ under ultraviolet light reach the maximum value, respectively.^{6,67} Amounts of r-GO and SnS₂ over 3% and 10%, respectively, lead to the degradation of photoreduction properties; this can be ascribed to excessive r-GO and SnS₂ adhesion on the MoS₂ surface will limit the photocatalytic semiconductor photoabsorption and reduce the contact area in the reactor–photocatalyst system.⁶⁸ In addition, the special structure of the MoS₂/SnS₂/r-GO van der Waals heterojunction can provide lower diffusion resistance and faster ion diffusion channels, and the interface synergy can improve electrochemical performance.²⁷ The same conclusion was obtained from ESR and PL analyses (Figures 6 and 8). Therefore, the enhanced photocatalytic properties with MoS₂/SnS₂/r-GO are attributed to the presence of r-GO and SnS₂, thanks to increasing charge carriers and usable exciters. According to the above analysis, it is indicated that MoS₂/10% SnS₂/3% r-GO has the highest activity for photoreduction of CO₂ under ultraviolet irradiation. The catalyst yields of CO and CH₄ after 5 h are shown in Table 1.

Further, in order to determine the source and content of the product during CO₂ photoreduction, an isotope tracer experiment was carried out by gas chromatography–mass spectrometry (GC-MS) for photoreduction of ¹³C and ¹²C on MoS₂/SnS₂/r-GO. The labeled CO₂ is analyzed as shown in Figure 9e,f. The overwhelming signals at *m/z* 17, 29 (¹³CH₄,

¹³CO) and *m/z* 16, 28 (¹²CH₄, ¹²CO) were clearly observed in the mass spectrum of the photocatalytic product, confirming that the detected reduction product was derived from MoS₂/SnS₂/r-GO photocatalytic CO₂ reduction. The results of the analysis are consistent with those in other literature.⁶⁹

3.9. Proposed Mechanism of Photoreduction. In the results discussed above, it is clear that the MoS₂/SnS₂/r-GO hybrid nanomaterials show a significant enhancement in the production of superoxide and hydroxyl and photoinduced cavities in comparison to MoS₂, SnS₂, MoS₂/r-GO photoactivity, which is consistent with the dispersibility of SnS₂ and the carbon-containing r-GO. It is worth noting that the r-GO provides both a fast channel for electron transport and a 2D structure of carbon for the MoS₂/SnS₂/r-GO heterojunction.⁴⁴ The platform plays a vital role in the photocatalytic performance. The empirical formulas for calculating the energy band position of the relevant materials MoS₂ and SnS₂ are $E_{VB} = X - E_c + 0.5E_g$ and $E_{CB} = E_{VB} - E_g$.³⁷ On the basis of the band gap energy calculated by DRS spectroscopy, the band gap energies of pure MoS₂ and pure SnS₂ (E_g) are estimated on the basis of the intercept of the tangent of the curve of $(ah\nu)^{1/2}$ (or $(ah\nu)^2$) and light energy. In Figure 4a the band gaps of pure MoS₂ and pure SnS₂ are 1.78 and 2.05 eV, respectively. In Figure S1a,b, the flat band potentials of pure MoS₂ and pure SnS₂ were tested by the Mott Nitro Curve, which were −0.15 and −0.55 eV, respectively, and the valence band positions of pure MoS₂ and pure SnS₂ were calculated by the formula as 1.63 and 1.50 eV, respectively. In addition, as shown in Figure 4b, the valence band position is further confirmed by XPS. The valence band spectrum shows that the valence band positions of pure MoS₂ and pure SnS₂ are 1.61 and 1.46 eV, respectively, which are basically consistent with the empirical calculation formula. Moreover, the VB and CB values of the semiconductor material determine the form and intensity of ROS generated by photoexcitation.^{59,70} MoS₂/SnS₂/r-GO has a lower CB value than $E_0(\text{O}_2/\bullet\text{O}_2^-)$ (−0.33 eV vs NHE) due to the enhanced superoxide radical strength of the composite. However, the CB of pure MoS₂ cannot produce superoxide; therefore, electrons can only migrate from the MoS₂ conduction band to the valence band of SnS₂. In addition, since MoS₂ and SnS₂ have overlapping band potentials, they can form effective Z-type heterojunctions.²⁸ Figure 10 shows a

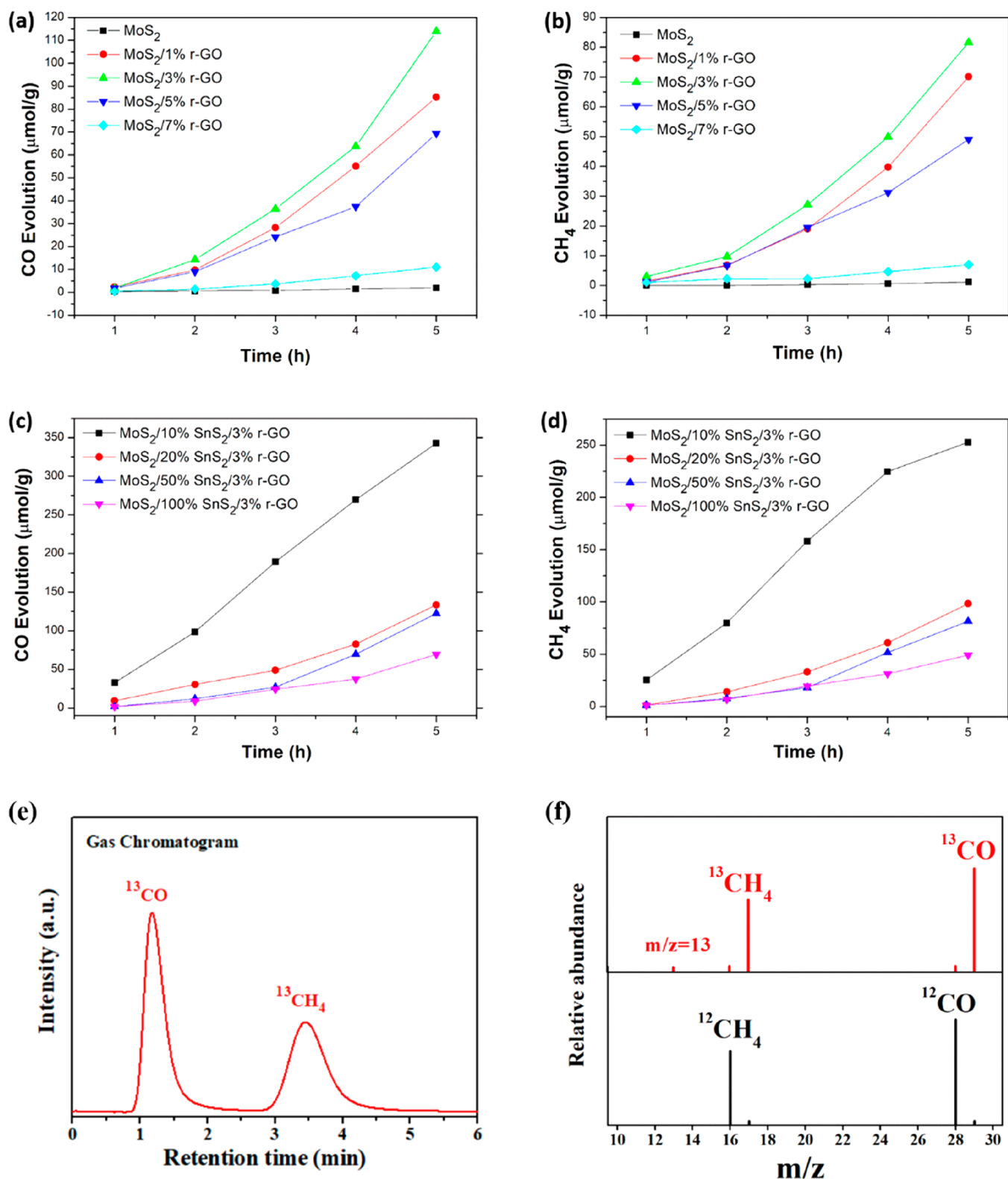


Figure 9. Reduction of CO₂ by MoS₂, MoS₂/r-GO, and MoS₂/SnS₂/r-GO under ultraviolet light: (a, c) CO production at 5 h; (b, d) CH₄ production at 5 h; (e, f) gas chromatography–mass spectrometry (GC-MS) analysis of CO and CH₄ produced by MoS₂/SnS₂/r-GO at 3 h.

detailed plot. Under ultraviolet light, electrons are easily excited from the MoS₂ conduction band (CB) to the valence band (VB) in SnS₂, producing photoelectron hole pairs.⁴⁴ Then, a part of the photogenerated electrons in SnS₂ undergoes reduction of CO₂, and another part of the photogenerated electrons and the electrons of the MoS₂

conduction band migrate to the surface of the r-GO to reduce CO₂ to CO and CH₄, thereby forming multilevel electron transport.⁷¹ At the same time, the holes of the MoS₂ valence band combine with the sacrificial agent EDTA to inhibit the recombination of photogenerated carriers, so that more photogenerated electrons participate in the process of

Table 1. Yield of CO and CH₄ (5 h) in Every Experiment with Different Catalysts

	photocatalyst		
	MoS ₂	MoS ₂ /3% r-GO	MoS ₂ /10% SnS ₂ /3% r-GO
yield of CO (μmol/g)	1.98	113.97	342.66
yield of CH ₄ (μmol/g)	1.15	81.61	252.74

photoreduction of CO₂, producing more organic compound fuel. In addition, the transfer of electrons and holes in the high-efficiency Z-type heterojunction can efficiently improve the separation of photoelectron hole pairs, inhibit their recombination, and prolong the lifetime, thereby improving the photocatalytic performance.⁷² Since r-GO has a short electronic transmission path and good electrical conductivity, electron–hole recombination is extremely limited. In addition, the uniform dispersion of MoS₂ and SnS₂ on r-GO provides more photocatalytic active sites for CO₂ gas reduction. Therefore, the performance of MoS₂/SnS₂/r-GO photocatalyst has been remarkably improved.

4. CONCLUSION

In summary, we have experimentally demonstrated the formation of MoS₂/SnS₂/r-GO by coupling during a synthesis. Representative detection of the photoexcitation process of MoS₂/SnS₂/r-GO has been fairly analyzed by photoluminescence spectroscopy. From the effective adjustment of the energy band structure of the r-GO-based material, the prepared MoS₂/SnS₂/r-GO showed significant optical excitation in photoactive oxygen (ROS), demonstrating that the superoxide radical ($\cdot\text{O}_2^-$) and hydroxyl radical ($\cdot\text{OH}$) are the main active substances under UV–visible irradiation, and the formed Z-type heterojunction has a multilevel electron transport mechanism, thereby increasing the efficiency of the reaction in the production of value-added fuel. This study provides an efficient and novel approach to the introduction of two-dimensional carbon materials. At the same time, it has also developed a new perspective for the synergy of heterojunctions with chalcogenide semiconductors, providing an advantageous

way to extend transition metal semiconductor based photo-reduction technology.

■ ASSOCIATED CONTENT

Supporting Information

The Supporting Information is available free of charge on the ACS Publications website at DOI: 10.1021/acs.inorgchem.9b02676.

Flat band potentials of pure MoS₂ and pure SnS₂ tested by the Mott Nitro Curve (PDF)

■ AUTHOR INFORMATION

Corresponding Authors

*E-mail for P.H.: huopw@mail.ujs.edu.cn.

*E-mail for H.W.: hqwang@mail.ujs.edu.cn.

ORCID

Pengwei Huo: 0000-0001-9647-7871

Yongsheng Yan: 0000-0001-7083-3292

Notes

The authors declare no competing financial interest.

■ ACKNOWLEDGMENTS

We gratefully acknowledge the financial support of the National Natural Science Foundation of China (Grant Nos. 21776117 and 21576125), China Postdoctoral Science Foundation (Grant Nos. 2017M611716 and 2017M611734), and Six talent peaks project in Jiangsu Province (Grant No. XCL-014).

■ REFERENCES

- (1) Liang, R.; Jing, F.; Shen, L.; Qin, N.; Wu, L. MIL-53(Fe) as a highly efficient bifunctional photocatalyst for the simultaneous reduction of Cr(VI) and oxidation of dyes. *J. Hazard. Mater.* **2015**, *287*, 364–372.
- (2) Peters, R. L. The Greenhouse Effect and Nature Reserves. *BioScience* **1985**, *35*, 707–717.
- (3) Li, J.; Ma, Y.; Ye, Z.; Zhou, M.; Wang, H.; Ma, C.; Wang, D.; Huo, P.; Yan, Y. Fast electron transfer and enhanced visible light photocatalytic activity using multi-dimensional components of carbon

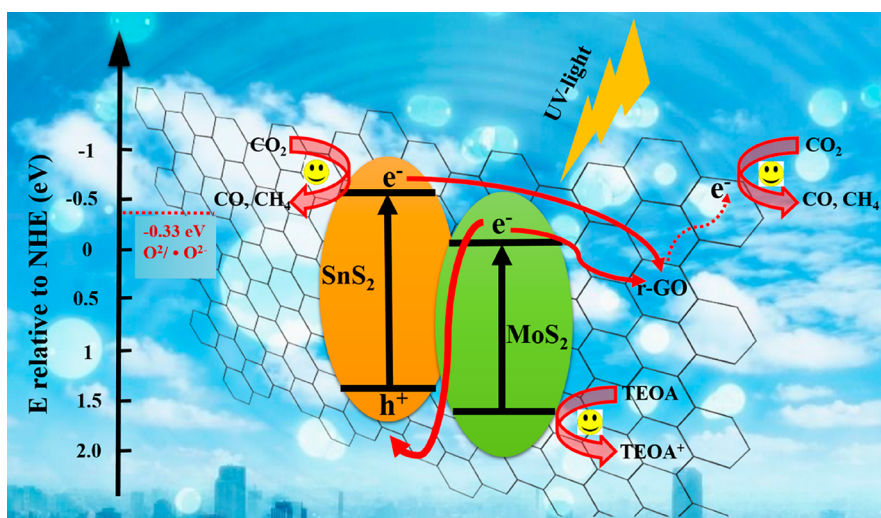


Figure 10. Mechanism of the figure of energy band structure and separation of charge mechanism during the photoreduction of the MoS₂/SnS₂/r-GO system under UV light irradiation.

- quantum dots@3D daisy-like In_2S_3 /single-wall carbon nanotubes. *Appl. Catal., B* **2017**, *204*, 224–238.
- (4) Fu, F.; Shen, H.; Sun, X.; Xue, W.; Shoneye, A.; Ma, J.; Luo, L.; Wang, D.; Wang, J.; Tang, J. Synergistic effect of surface oxygen vacancies and interfacial charge transfer on Fe(III)/ Bi_2MoO_6 for efficient photocatalysis. *Appl. Catal., B* **2019**, *247*, 150–162.
- (5) Morais, D. F. S.; Boaventura, R. A. R.; Moreira, F. C.; Vilar, V. J. P. Advances in bromate reduction by heterogeneous photocatalysis: The use of a static mixer as photocatalyst support. *Appl. Catal., B* **2019**, *249*, 322–332.
- (6) Chen, W.; Han, B.; Tian, C.; Liu, X.; Liang, S.; Deng, H.; Lin, Z. MOFs-derived ultrathin holey Co_3O_4 nanosheets for enhanced visible light CO_2 reduction. *Appl. Catal., B* **2019**, *244*, 996–1003.
- (7) Meier, A. J.; Garg, A.; Sutter, B.; Kuhn, J. N.; Bhethanabotla, V. R. MoS_2 Nanoflowers as a Gateway for Solar-Driven CO_2 Photoreduction. *ACS Sustainable Chem. Eng.* **2019**, *7*, 265–275.
- (8) Che, H.; Che, P.; Zhou, G.; Liu, C.; Dong, H.; Li, C.; Song, N.; Li, C. Nitrogen doped carbon ribbons modified g-C $_3$ N $_4$ for markedly enhanced photocatalytic H_2 -production in visible to near-infrared region. *Chem. Eng. J.* **2020**, *382*, 122870.
- (9) Coy-Diaz, H.; Bertran, F.; Chen, C.; Avila, J.; Rault, J.; Le Fèvre, P.; Asensio, M. C.; Bätzill, M. Band renormalization and spin polarization of MoS_2 in graphene/ MoS_2 heterostructures. *Phys. Status Solidi RRL* **2015**, *9*, 701–706.
- (10) Jiang, Y.; Peng, Y.; Xi, B.; Kai, S.; Mi, K.; Feng, J.; Zhang, J.; Xiong, S. Ultrasmall SnS_2 nanoparticles anchored on well-distributed nitrogen-doped graphene sheets for Li-ion and Na-ion batteries. *J. Mater. Chem. A* **2016**, *4*, 10719–10726.
- (11) Oakes, L.; Carter, R.; Hanken, T.; Cohn, A. P.; Share, K.; Schmidt, B.; Pint, C. L. Interface strain in vertically stacked two-dimensional heterostructured carbon- MoS_2 nanosheets controls electrochemical reactivity. *Nat. Commun.* **2016**, *7*, 11796.
- (12) Teng, Y.; Zhao, H.; Zhang, Z.; Li, Z.; Xia, Q.; Zhang, Y.; Zhao, L.; Du, X.; Du, Z.; Lv, P.; Swierczek, K. MoS_2 Nanosheets Vertically Grown on Graphene Sheets for Lithium-Ion Battery Anodes. *ACS Nano* **2016**, *10*, 8526–8535.
- (13) Liu, Y.; Li, Y.; Peng, F.; Lin, Y.; Yang, S.; Zhang, S.; Wang, H.; Cao, Y.; Yu, H. 2H- and 1T- mixed phase few-layer MoS_2 as a superior to Pt co-catalyst coated on TiO_2 nanorod arrays for photocatalytic hydrogen evolution. *Appl. Catal., B* **2019**, *241*, 236–245.
- (14) Bai, X.; Du, Y.; Hu, X.; He, Y.; He, C.; Liu, E.; Fan, J. Synergy removal of Cr (VI) and organic pollutants over RP- MoS_2 /rGO photocatalyst. *Appl. Catal., B* **2018**, *239*, 204–213.
- (15) Liu, J.; Liu, Y.; Xu, D.; Zhu, Y.; Peng, W.; Li, Y.; Zhang, F.; Fan, X. Hierarchical “nanoroll” like MoS_2 / $\text{Ti}_3\text{C}_2\text{Tx}$ hybrid with high electrocatalytic hydrogen evolution activity. *Appl. Catal., B* **2019**, *241*, 89–94.
- (16) Li, X.; Lv, X.; Li, N.; Wu, J.; Zheng, Y.-Z.; Tao, X. One-step hydrothermal synthesis of high-percentage 1T-phase MoS_2 quantum dots for remarkably enhanced visible-light-driven photocatalytic H_2 evolution. *Appl. Catal., B* **2019**, *243*, 76–85.
- (17) Wang, Y.; Zhang, Z.; Zhang, L.; Luo, Z.; Shen, J.; Lin, H.; Long, J.; Wu, J. C. S.; Fu, X.; Wang, X.; Li, C. Visible-Light Driven Overall Conversion of CO_2 and H_2O to CH_4 and O_2 on 3D-SiC@2D- MoS_2 Heterostructure. *J. Am. Chem. Soc.* **2018**, *140*, 14595–14598.
- (18) Liu, Z.; Zhao, L.; Liu, Y.; Gao, Z.; Yuan, S.; Li, X.; Li, N.; Miao, S. Vertical nanosheet array of 1T phase MoS_2 for efficient and stable hydrogen evolution. *Appl. Catal., B* **2019**, *246*, 296–302.
- (19) Bremmer, G. M.; van Haandel, L.; Hensen, E. J. M.; Frenken, J. W. M.; Kooyman, P. J. The effect of oxidation and resulfidation on (Ni/Co) MoS_2 hydrodesulfurisation catalysts. *Appl. Catal., B* **2019**, *243*, 145–150.
- (20) Stolarczyk, J. K.; Bhattacharyya, S.; Polavarapu, L.; Feldmann, J. Challenges and Prospects in Solar Water Splitting and CO_2 Reduction with Inorganic and Hybrid Nanostructures. *ACS Catal.* **2018**, *8*, 3602–3635.
- (21) Wu, C.; Zhou, Y.; Zou, Z. Research Progress in Photocatalytic Conversion of CO_2 to Hydrocarbons. *Cuihua Xuebao* **2013**, *32*, 1565–1572.
- (22) Jiao, X.; Li, X.; Jin, X.; Sun, Y.; Xu, J.; Liang, L.; Ju, H.; Zhu, J.; Pan, Y.; Yan, W.; Lin, Y.; Xie, Y. Partially Oxidized SnS_2 Atomic Layers Achieving Efficient Visible-Light-Driven CO_2 Reduction. *J. Am. Chem. Soc.* **2017**, *139*, 18044–18051.
- (23) Zhang, F.; Zhang, Y.; Zhang, G.; Yang, Z.; Dionysiou, D. D.; Zhu, A. Exceptional synergistic enhancement of the photocatalytic activity of SnS_2 by coupling with polyaniline and N-doped reduced graphene oxide. *Appl. Catal., B* **2018**, *236*, 53–63.
- (24) Zhang, Z.; Huang, J.; Zhang, M.; Yuan, Q.; Dong, B. Ultrathin hexagonal SnS_2 nanosheets coupled with g-C $_3$ N $_4$ nanosheets as 2D/2D heterojunction photocatalysts toward high photocatalytic activity. *Appl. Catal., B* **2015**, *163*, 298–305.
- (25) Qu, J.; Chen, D.; Li, N.; Xu, Q.; Li, H.; He, J.; Lu, J. Coral-inspired nanoscale design of porous SnS_2 for photocatalytic reduction and removal of aqueous Cr (VI). *Appl. Catal., B* **2017**, *207*, 404–411.
- (26) Parveen, N.; Ansari, S. A.; Alamri, H. R.; Ansari, M. O.; Khan, Z.; Cho, M. H. Facile Synthesis of SnS_2 Nanostructures with Different Morphologies for High-Performance Supercapacitor Applications [J]. *ACS Omega* **2018**, *3* (2), 1581–1588.
- (27) Man, X.; Liang, P.; Shu, H.; Zhang, L.; Wang, D.; Chao, D.; Liu, Z.; Du, X.; Wan, H.; Wang, H. Interface Synergistic Effect from Layered Metal Sulfides of MoS_2 / SnS_2 van der Waals Heterojunction with Enhanced Li-Ion Storage Performance. *J. Phys. Chem. C* **2018**, *122*, 24600–24608.
- (28) Wang, H.; Zhang, L.; Chen, Z.; Hu, J.; Li, S.; Wang, Z.; Liu, J.; Wang, X. Semiconductor heterojunction photocatalysts: design, construction, and photocatalytic performances. *Chem. Soc. Rev.* **2014**, *43*, 5234–5244.
- (29) Chang, K.; Mei, Z.; Wang, T.; Kang, Q.; Ouyang, S.; Ye, J. MoS_2 /graphene cocatalyst for efficient photocatalytic H_2 evolution under visible light irradiation. *ACS Nano* **2014**, *8*, 7078–7087.
- (30) Hummers, W. S.; Offeman, R. E. Preparation of Graphitic Oxide. *J. Am. Chem. Soc.* **1958**, *80* (6), 1339.
- (31) Li, X.; Zhu, J.; Li, H. Comparative study on the mechanism in photocatalytic degradation of different-type organic dyes on SnS_2 and CdS. *Appl. Catal., B* **2012**, *123–124*, 174–181.
- (32) Zang, S.; Zhang, G.; Lan, Z.-A.; Zheng, D.; Wang, X. Enhancement of photocatalytic H_2 evolution on pyrene-based polymer promoted by MoS_2 and visible light. *Appl. Catal., B* **2019**, *251*, 102–111.
- (33) Zhang, Y. C.; Yao, L.; Zhang, G.; Dionysiou, D. D.; Li, J.; Du, X. One-step hydrothermal synthesis of high-performance visible-light-driven SnS_2 / SnO_2 nanoheterojunction photocatalyst for the reduction of aqueous Cr(VI). *Appl. Catal., B* **2014**, *144*, 730–738.
- (34) Zhang, X.; Zhang, P.; Wang, L.; Gao, H.; Zhao, J.; Liang, C.; Hu, J.; Shao, G. Template-oriented synthesis of monodispersed SnS_2 @ SnO_2 hetero-nanoflowers for Cr(VI) photoreduction. *Appl. Catal., B* **2016**, *192*, 17–25.
- (35) Che, H.; Liu, L.; Che, G.; Dong, H.; Liu, C.; Li, C. Control of energy band, layer structure and vacancy defect of graphitic carbon nitride by intercalated hydrogen bond effect of NO_3^- toward improving photocatalytic performance. *Chem. Eng. J.* **2019**, *357*, 209–219.
- (36) Pan, Y. X.; You, Y.; Xin, S.; Li, Y.; Fu, G.; Cui, Z.; Men, Y. L.; Cao, F. F.; Yu, S. H.; Goodenough, J. B. Photocatalytic CO_2 Reduction by Carbon-Coated Indium-Oxide Nanobelts. *J. Am. Chem. Soc.* **2017**, *139*, 4123–4129.
- (37) Chen, C.; Cai, W.; Long, M.; Zhou, B.; Wu, Y.; Wu, D.; Feng, Y. Synthesis of visible-light responsive graphene oxide/ TiO_2 (2) composites with p/n heterojunction. *ACS Nano* **2010**, *4*, 6425–6432.
- (38) Hu, X.; Lu, S.; Tian, J.; Wei, N.; Song, X.; Wang, X.; Cui, H. The selective deposition of MoS_2 nanosheets onto (101) facets of TiO_2 nanosheets with exposed (001) facets and their enhanced photocatalytic H_2 production. *Appl. Catal., B* **2019**, *241*, 329–337.
- (39) Tong, Z.; Yan, C.; Su, Z.; Zeng, F.; Yang, J.; Li, Y.; Jiang, L.; Lai, Y.; Liu, F. Effects of potassium doping on solution processed

- kesterite $\text{Cu}_2\text{ZnSnS}_4$ thin film solar cells. *Appl. Phys. Lett.* **2014**, *105*, 223903–4.
- (40) Li, Z.; Zhou, Z.; Ma, J.; Li, Y.; Peng, W.; Zhang, G.; Zhang, F.; Fan, X. Hierarchical photocatalyst of In_2S_3 on exfoliated MoS_2 nanosheets for enhanced visible-light-driven Aza-Henry reaction. *Appl. Catal., B* **2018**, *237*, 288–294.
- (41) Parzinger, E.; Miller, B.; Blaschke, B.; Garrido, J. A.; Ager, J. W.; Holleitner, A.; Wurstbauer, U. Photocatalytic Stability of Single- and Few-Layer MoS_2 [J]. *ACS Nano* **2015**, *9* (11), 11302–11309.
- (42) Jiang, Y.; Guo, Y.; Lu, W.; Feng, Z.; Xi, B.; Kai, S.; Zhang, J.; Feng, J.; Xiong, S. Rationally Incorporated $\text{MoS}_2/\text{SnS}_2$ Nanoparticles on Graphene Sheets for Lithium-Ion and Sodium-Ion Batteries. *ACS Appl. Mater. Interfaces* **2017**, *9*, 27697–27706.
- (43) Pang, Y.; Zhang, S.; Liu, L.; Liang, J.; Sun, Z.; Wang, Y.; Xiao, C.; Ding, D.; Ding, S. Few-layer MoS_2 anchored at nitrogen-doped carbon ribbons for sodium-ion battery anodes with high rate performance. *J. Mater. Chem. A* **2017**, *5*, 17963–17972.
- (44) Wu, M.-h.; Li, L.; Xue, Y.-c.; Xu, G.; Tang, L.; Liu, N.; Huang, W.-y. Fabrication of ternary $\text{GO}/\text{g-C}_3\text{N}_4/\text{MoS}_2$ flower-like heterojunctions with enhanced photocatalytic activity for water remediation. *Appl. Catal., B* **2018**, *228*, 103–112.
- (45) Suzuki, K.; Malfatti, L.; Carboni, D.; Loche, D.; Casula, M.; Moretto, A.; Maggini, M.; Takahashi, M.; Innocenzi, P. Energy Transfer Induced by Carbon Quantum Dots in Porous Zinc Oxide Nanocomposite Films. *J. Phys. Chem. C* **2015**, *119*, 2837–2843.
- (46) Hao, X.; Jin, Z.; Yang, H.; Lu, G.; Bi, Y. Peculiar synergetic effect of MoS_2 quantum dots and graphene on Metal-Organic Frameworks for photocatalytic hydrogen evolution. *Appl. Catal., B* **2017**, *210*, 45–56.
- (47) Li, J.; Pei, Q.; Wang, R.; Zhou, Y.; Zhang, Z.; Cao, Q.; Wang, D.; Mi, W.; Du, Y. Enhanced Photocatalytic Performance through Magnetic Field Boosting Carrier Transport. *ACS Nano* **2018**, *12*, 3351–3359.
- (48) Liu, G.; Wang, L.; Sun, C.; Yan, X.; Wang, X.; Chen, Z.; Smith, S.; Cheng, H.; Lu, G. Band-to-band visible-light photon excitation and photoactivity induced by homogeneous nitrogen doping in layered titanates[J]. *Chem. Mater.* **2009**, *21* (7), 1266–1274.
- (49) Lu, Y.; Zhang, J.; Wang, F.; Chen, X.; Feng, Z.; Li, C. K_2SO_4 -Assisted Hexagonal/Monoclinic WO_3 Phase Junction for Efficient Photocatalytic Degradation of RhB. *ACS Appl. Energy Mater.* **2018**, *1*, 2067–2077.
- (50) Li, J.; Liu, K.; Xue, J.; Xue, G.; Sheng, X.; Wang, H.; Huo, P.; Yan, Y. CQDs preluded carbon-incorporated 3D burger-like hybrid ZnO enhanced visible-light-driven photocatalytic activity and mechanism implication. *J. Catal.* **2019**, *369*, 450–461.
- (51) David, L.; Bhandavat, R.; Singh, G. MoS_2 /graphene composite paper for sodium-ion battery electrodes. *ACS Nano* **2014**, *8*, 1759–1770.
- (52) Sun, S.; Li, X.; Wang, W.; Zhang, L.; Sun, X. Photocatalytic robust solar energy reduction of dinitrogen to ammonia on ultrathin MoS_2 [J]. *Appl. Catal., B* **2017**, *200*, 323–329.
- (53) Li, H.; He, X.; Kang, Z.; Huang, H.; Liu, Y.; Liu, J.; Lian, S.; Tsang, C. H. A.; Yang, X.; Lee, S.-T. Water-Soluble Fluorescent Carbon Quantum Dots and Photocatalyst Design. *Angew. Chem., Int. Ed.* **2010**, *49*, 4430–4434.
- (54) Li, X.; Rui, M.; Song, J.; Shen, Z.; Zeng, H. Carbon and Graphene Quantum Dots for Optoelectronic and Energy Devices: A Review. *Adv. Funct. Mater.* **2015**, *25*, 4929–4947.
- (55) Zhang, L.; Cheng, H.; Zong, R.; Zhu, Y. Photocorrosion Suppression of ZnO Nanoparticles via Hybridization with Graphite-like Carbon and Enhanced Photocatalytic Activity. *J. Phys. Chem. C* **2009**, *113*, 2368–2374.
- (56) Hong, S. Y.; Popovitz-Biro, R.; Prior, Y.; Tenne, R. Synthesis of SnS_2/SnS fullerene-like nanoparticles: a superlattice with polyhedral shape. *J. Am. Chem. Soc.* **2003**, *125*, 10470–10474.
- (57) Becerril, H. A.; Stoltenberg, R. M.; Tang, M. L.; Roberts, M. E.; Liu, Z.; Chen, Y.; Kim, D. H.; Lee, B. L.; Lee, S.; Bao, Z. Fabrication and evaluation of solution-processed reduced graphene oxide electrodes for p- and n-channel bottom-contact organic thin-film transistors. *ACS Nano* **2010**, *4*, 6343–6352.
- (58) Meng, F.; Li, J.; Cushing, S. K.; Zhi, M.; Wu, N. Solar hydrogen generation by nanoscale p–n junction of p-type molybdenum disulfide/n-type nitrogen-doped reduced graphene oxide. *J. Am. Chem. Soc.* **2013**, *135*, 10286–10289.
- (59) Xu, J.; Wang, Z.; Zhu, Y. Enhanced Visible-Light-Driven Photocatalytic Disinfection Performance and Organic Pollutant Degradation Activity of Porous $\text{g-C}_3\text{N}_4$ Nanosheets. *ACS Appl. Mater. Interfaces* **2017**, *9*, 27727–27735.
- (60) Chauhan, H.; Soni, K.; Kumar, M.; Deka, S. Tandem Photocatalysis of Graphene-Stacked SnS_2 Nanodiscs and Nanosheets with Efficient Carrier Separation. *ACS Omega* **2016**, *1*, 127–137.
- (61) Zhou, M.; Han, D.; Liu, X.; Ma, C.; Wang, H.; Tang, Y.; Huo, P.; Shi, W.; Yan, Y.; Yang, J. Enhanced visible light photocatalytic activity of alkaline earth metal ions-doped CdSe/rGO photocatalysts synthesized by hydrothermal method. *Appl. Catal., B* **2015**, *172–173*, 174–184.
- (62) Zhou, M.; Li, J.; Ye, Z.; Ma, C.; Wang, H.; Huo, P.; Shi, W.; Yan, Y. Transfer Charge and Energy of $\text{Ag}@\text{CdSe}$ QDs-rGO Core-Shell Plasmonic Photocatalyst for Enhanced Visible Light Photocatalytic Activity. *ACS Appl. Mater. Interfaces* **2015**, *7*, 28231–28243.
- (63) Wang, H.; Yang, X.; Shao, W.; Chen, S.; Xie, J.; Zhang, X.; Wang, J.; Xie, Y. Ultrathin Black Phosphorus Nanosheets for Efficient Singlet Oxygen Generation. *J. Am. Chem. Soc.* **2015**, *137*, 11376–11382.
- (64) He, W.; Kim, H. K.; Wamer, W. G.; Melka, D.; Callahan, J. H.; Yin, J. J. Photogenerated charge carriers and reactive oxygen species in ZnO/Au hybrid nanostructures with enhanced photocatalytic and antibacterial activity. *J. Am. Chem. Soc.* **2014**, *136*, 750–757.
- (65) Li, Q.; Zhang, N.; Yang, Y.; Wang, G.; Ng, D. H. High efficiency photocatalysis for pollutant degradation with $\text{MoS}_2/\text{C}_3\text{N}_4$ heterostructures. *Langmuir* **2014**, *30*, 8965–8972.
- (66) Iwase, A.; Yoshino, S.; Takayama, T.; Ng, Y. H.; Amal, R.; Kudo, A. Water Splitting and CO_2 Reduction under Visible Light Irradiation Using Z-Scheme Systems Consisting of Metal Sulfides, CoO_x -Loaded BiVO_4 , and a Reduced Graphene Oxide Electron Mediator. *J. Am. Chem. Soc.* **2016**, *138*, 10260–10264.
- (67) Li, Y.; Wang, C.; Song, M.; Li, D.; Zhang, X.; Liu, Y. $\text{TiO}_{2-x}/\text{CoO}_x$ photocatalyst sparkles in photothermocatalytic reduction of CO_2 with H_2O steam. *Appl. Catal., B* **2019**, *243*, 760–770.
- (68) Di, J.; Xia, J.; Ge, Y.; Li, H.; Ji, H.; Xu, H.; Zhang, Q.; Li, H.; Li, M. Novel visible-light-driven CQDs/ Bi_2WO_6 hybrid materials with enhanced photocatalytic activity toward organic pollutants degradation and mechanism insight[J]. *Appl. Catal., B* **2015**, *168–169*, 51–61.
- (69) Bie, C.; Zhu, B.; Xu, F.; Zhang, L.; Yu, J. In Situ Grown Monolayer N-Doped Graphene on CdS Hollow Spheres with Seamless Contact for Photocatalytic CO_2 Reduction. *Adv. Mater.* **2019**, *31*, 1902868.
- (70) Cui, W.; He, J.; Wang, H.; Hu, J.; Liu, L.; Liang, Y. Polyaniline hybridization promotes photo-electro-catalytic removal of organic contaminants over 3D network structure of $\text{rGH-PANI}/\text{TiO}_2$ hydrogel. *Appl. Catal., B* **2018**, *232*, 232–245.
- (71) Schmidt, H. C.; Reuter, L. G.; Hamacek, J.; Wenger, O. S. Multistage complexation of fluoride ions by a fluorescent triphenylamine bearing three dimethylboron groups: controlling intramolecular charge transfer. *J. Org. Chem.* **2011**, *76*, 9081–9085.
- (72) Wang, S.; Guan, B. Y.; Lou, X. W. D. Construction of ZnIn_2S_4 - In_2O_3 Hierarchical Tubular Heterostructures for Efficient CO_2 Photoreduction. *J. Am. Chem. Soc.* **2018**, *140*, 5037–5040.